PUBLICATIONS OF THE ASTRONOMICAL SOCIETY OF THE PACIFIC, **123**:448–460, 2011 April

FlyEyes: A CCD-based Wavefront Sensor for PUEO, the CFHT Curvature AO System

OLIVIER LAI, JEAN-CHARLES CUILLANDRE, KEVIN K. Y. HO, MARC BARIL, TOM BENEDICT, JEFF WARD, JIM THOMAS, AND DERRICK SALMON

Canada-France-Hawaii Telescope, 65-1238 Mamalahoa Highway, Kamuela, HI 96743

CHUEH-JEN LIN, AND SHIANG-YU WANG

Institute for Astronomy and Astrophysics, National Taiwan University, Taipei 10617, Taiwan, R.O.C.

GERRY LUPPINO

GL Scientific, 3367 Waialae Avenue, Honolulu, HI 96816

REINHOLD DORN

European Southern Observatory, Karl-Schwarzschild Strasse 2, 85748 Garching bei Munchen, Germany

PASCAL PUGET

Laboratoire d'Astrophysique de l'Observatoire de Grenoble, BP 53, F-38041 Grenoble, France

BARRY BURKE

MIT Lincoln Laboratory, 244 Wood Street, Lexington, MA 02420-9108

AND

JAMES BELETIC

Teledyne Imaging Sensors, Camarillo, CA 93102

Received 2010 November 3; accepted 2011 January 12; published 2011 March 1

ABSTRACT. Adaptive optics wavefront sensing imposes stringent requirements on detectors, due to the simultaneous need for extremely low read noise and high frame rates. Curvature wavefront sensing measurements are based on the normalized intensity of the signal in a given subaperture, and avalance photodiodes (APDs) have traditionally been used as detectors in curvature systems such as the Canada-France-Hawaii Telescope (CFHT) adaptive optics (AO) bonnette, called PUEO after the endemic Hawaiian owl. Passively quenched APDs are robust but have low QE ($\sim 40\%$), while actively quenched APDs can have much higher QE, but have been known to fail. Furthermore, curvature systems with large numbers of subapertures are now in operation, and the cost of individual APDs may become prohibitive for such systems. Thus, a CCD-based alternative appears very attractive, and development of a specific chip was initiated at ESO 10 years ago. In this article, we report on the performance of the FlyEyes camera, a project that was conceived to compare the performance of the backside-illuminated custom-designed CCD detector with an array of APDs, used in an operational and well-characterized curvature wavefront AO system. The on-sky performance is demonstrated to be unaffected on bright guide stars (i.e., negligible latency), and although the faint end suffers from the $2.5\ e^-$ read noise, the performance can be regained by lowering the frame rate on the wavefront sensor. In this article, we report on results that show that the CCD can be used to replace an array of expensive APDs. This would enable a cost-effective upgrade of PUEO to a higher-order system, as has been proposed at various occasions.

Online material: color figures

1. INTRODUCTION

Curvature wavefront sensing adaptive optics (AO) systems continue to be used and developed with excellent results at many facilities; e.g., MACAO, SINFONI, CRIRES at ESO, NICI at Gemini, and C-188 at Subaru (see, e.g., Racine 2006). A clear advantage of curvature wavefront sensing is its normalized intensity measurement scheme, which allows single-pixel photon-counting detectors within each subaperture and avoids

the need to generate and measure an image, using complex optics as in a Shack-Hartmann wavefront sensor (WFS). Avalanche photodiodes (APDs) have traditionally been used as detectors for curvature WFSs, but their quantum efficiency (on the order of 40% for passively quenched APDs), cost, and failure rate (particularly for actively quenched APDs) suggests that developing a CCD-based detector for curvature sensing would be a useful endeavor.

Photon-counting and read-noise-less CCD detectors such as an electron-multiplying CCD (EMCCD) would fulfill a similar goal, although most likely in a different implementation. They have long been anticipated and are starting to become available for astronomical wavefront sensing applications (e.g., OCam; see Feautrier et al. 2010). Also, the use of fibers is not optimal, but it allows a match of the annular geometry of the lenslet array (and of the deformable mirror's electrode pattern) to square pixels. Radial CCDs are under development, especially to deal with the laser guide star elongation issue in extremely large telescopes (e.g., Thomas et al. 2007), but are not optimized for curvature sensing. Thus, the development by ESO and MIT Lincoln Laboratory (MIT/LL) of low-noise CCDs that are specifically tailored to curvature sensing was of particular interest to the Canada-France-Hawaii Telescope (CFHT), as its current AO system, PUEO, being fiber-fed, offered a perfect platform to test such a system in anticipation that its user community should decide to upgrade to a higher-order system (Lai et al. 2003; Lai 2004). This led to the development of the FlyEyes detector, which consists of two fiber-fed MIT/LL CCID-35 CCD arrays inside a dewar, and was intended for direct comparison with the APDs in PUEO as a swappable unit (Cuillandre et al. 2003; Ho et al. 2004, Ho et al. 2006). This article describes the final system as integrated in PUEO and the results of on-sky testing. The remainder of this section describes the CFHT AO system, PUEO, and the CCID-35 detector. Section 2 describes the FlyEyes camera and its implementation and the goals of the FlyEyes project. Simulations to estimate the expected performance and study the modes of operations of FlyEyes in different flux levels are presented in §§ 3, and 4 contains the results of on-sky results and comparison with the APDs. Section 5 concludes by summarizing and outlining the potential use of the FlyEyes detector.

1.1. PUEO

The CFHT adaptive optics system, PUEO, has been in service since first light in 1996 and continues to see routine usage. A full description of PUEO and its performance can be found in Rigaut et al. (1998). PUEO is based on curvature wavefront sensing with a 19-element bimorph deformable mirror and 19 passively quenched APDs. Light from the wavefront is divided into 19 subpupils by a lenslet array and fed via optical fibers to the APDs, which do the photon counting. FlyEyes replaces the APDs with two CCID-35 CCD detectors and an SDSU2 controller. The optical fibers are removed from the APDs and rerouted to the CCID-35s. The CCID-35 detectors, conceived at ESO and MIT/LL, were specifically tailored for use in curvature wavefront sensing (Beletic et al. 2000; Dorn 2001). A block diagram of PUEO illustrating how the CCID-35s integrate into PUEO is shown in Figure 1. A more detailed explanation of the FlyEyes concept is given in Cuillandre et al. (2003) and Ho et al. (2004).

1.2. CCID-35

The CCID-35 device was developed by ESO in collaboration with the MIT/LL fabrication facility (Beletic et al. 2000; Dorn 2001). One of its unique design features are "storage" areas on either side of the imaging array that are used to integrate charge from the intrafocal and extrafocal images used in curvature wavefront sensing. Having the storage areas eliminates the need to read out the images at each half-cycle of the membrane mirror intra- and extrafocal modulation (4 kHz in PUEO). The images can be clocked out at the full 1 kHz sampling rate, or at a lower divisor-of-2 rate (e.g., 500 or 250 Hz) when observing faint guide stars.

The curvature sensing area of the CCID-35 consists of eight columns nominally divided into 10 cells, with an additional eight-cell column that can be used for tip/tilt sensing (not used in CFHT PUEO), Figure 2 (*top*). Nominally, each cell consists of a 20×20 pixel imaging area (pixel sizes of 18×18 μm). Each column has its own serial output register and output amplifier allowing rapid readout of the array. Figure 2 (*bottom*) shows a diagram of the unit cell. Craven-Bartle et al. (2000) and Dorn (2001) found from simulations that the maximum acceptable read noise must be less than 2 e^- for the CCID-35 to provide a viable replacement for APDs. They successfully developed and tested a system at ESO with readout noise less than this value using front-illuminated versions of these devices (Dorn 2001). The detectors are operated at -100°C. Dark current is not a concern, given that exposure times are always less than 4 ms.

The device uses three-phase clocks for charge transfer. In Figure 2, storage areas SA and SB store the charge for the half-cycle intrafocal (I) and extrafocal (E) images. The storage area SC is used to temporarily hold the charge as one half-cycle image is clocked out through the serial output register. Charge is binned into a superpixel at the summing well before being output at the source follower amplifier.

The need for the storage area SC may not be immediately obvious, as the output register could be used to store the charge to be read out. However, since there may, in general, be several intra/extrafocal cycles between each sampling of the intra/extrafocal signals, the storage register SC is required to store the A phase signal during completion of the readout of the previous B phase signal located in the output serial register.

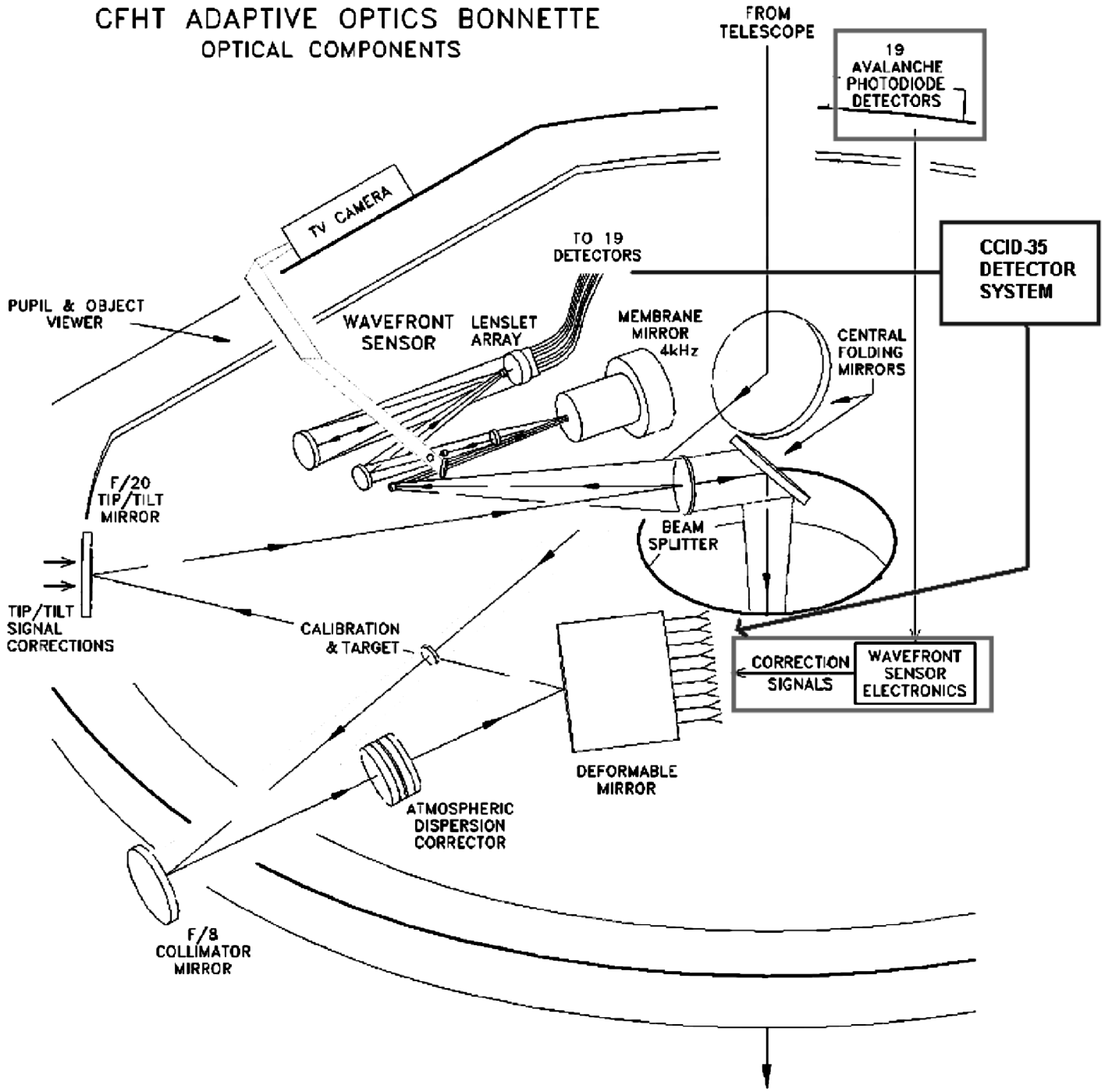

FIG. 1.—APD and CCID-35 paths are shown in this diagram of PUEO. The fibers are disconnected from the APDs and connected to the CCID-35. Instead of the digitized sum and difference counters from the analog WFS electronics, the real-time computer now receives values from a dedicated interface board. See the electronic edition of the *PASP* for a color version of this figure.

2. FLYEYES EXPERIMENT

Originally designed for a high-order curvature system with 104 subapertures, the wavefront sensor camera required two identical CCID-35 chips (since each one has 80 superpixels) housed in a single dewar, fed by fibers, which suggested the name "FlyEyes." Irrespective of the eventual outcome of the high-order system, it was decided to compare this camera with the APDs to determine whether these detectors could compete with APDs in an operational environment. Therefore, the FlyEyes project was designed to use the existing software,

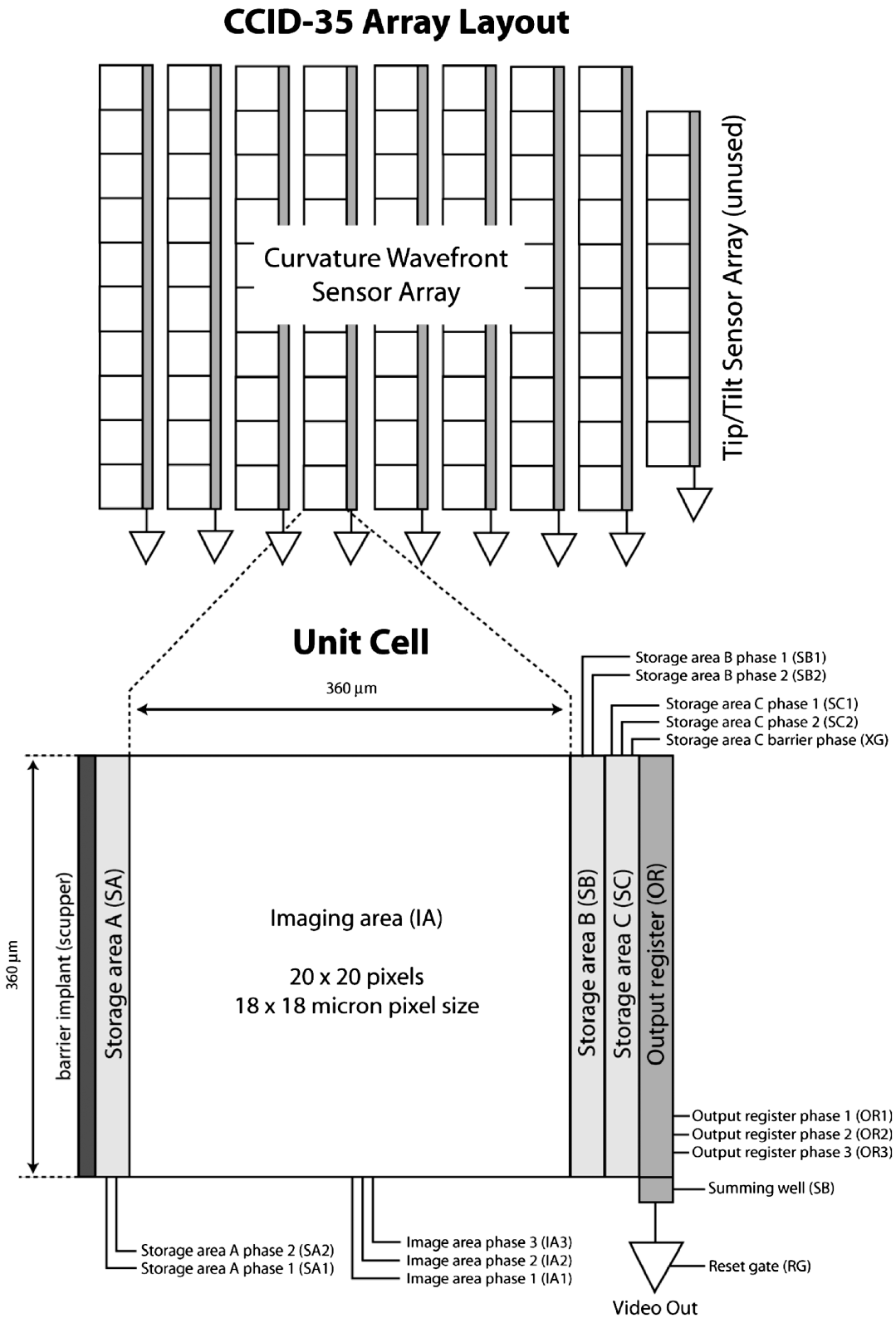

FIG. 2.—Architecture of the CCID-35 wavefront sensing CCD. *Top*: Array layout of 10×8 cells (superpixels), plus the eight unused cells for tip-tilt sensing on the right. *Bottom*: unit cell, with the SA storage area on left and SB and SC storage areas on right of central integration area.

hardware, and interfaces and to make no modifications to the existing hardware, such that the system could be restored to its original condition. Furthermore, the capability to switch between APDs and the CCID-35 so that side-by-side comparison testing could be done—if not during the night, at least on consecutive nights—was deemed desirable. And, of course, the base performance goal was to be able to maintain the current AO control-loop performance (>80 Hz loop bandwidth at 1 kHz sample rate).

A photograph of the system on the telescope is presented in Figure 3. Two CCID-35s are mounted in a liquid-nitrogen-cooled cryostat. Light from the lenslet array is brought into the cryostat via optical fibers. A SDSU2 controller from Astronomical Research Cameras, Inc., provides the clocks and biases for the CCDs. Four video processor boards with dual channels handle the amplification and digitization of the eight video channels from the CCD. (Only 19 cells [one for each subaperture of PUEO] distributed over four columns [to use all the amplifiers] are used in PUEO FlyEyes.) The SDSU2, which sits next to the cryostat mounted on the outside skin of the AO bonnette, transmits the readout data via fiber to the data-acquisition PC in the computer room (roughly 70 m from the telescope). A custom interface board ties in the existing interfaces to the SDSU2 controller and data-acquisition PC. This board performs address and control signal multiplexing between the digital I/O board in the data-acquisition PC and the existing WFS board. It also generates a synchronization signal from the 4 kHz clock that is used to synchronize timing patterns between the SDSU2 controller and the membrane mirror.

The data-acquisition PC is a dual-processor 2 GHz machine running real-time Linux. The PC processes the readout data from the SDSU2, which are summed and differenced and then made available to the LaserDot real-time computer (RTC) through the custom interface board. The LaserDot RTC reads and normalizes the intensities, computes the control matrix, and outputs actuator drive commands to the deformable mirror.

2.1. Fiber Bundle

As briefly mentioned in § 1.1, the fibers are disconnected from the APDs and rerouted to the CCID-35 cryostat through a vacuum feedthrough flange. Internal fibers direct the light onto the CCID-35 detector. By far, the most challenging aspect of the project was construction of the optical fiber bundle. The bundle required a minimum 19 fibers, one per each APD channel. The CCID-35 supports 80 fibers, one per each unit cell, which is much more than needed for PUEO. Building an 80-fiber bundle was deemed excessive for our needs, so a 54-fiber bundle was settled upon. This 9×6 layout was largely determined by the V grooves available to us, but provided a sufficient number of spares and also an opportunity to gain experience in constructing and testing a large fiber bundle, similar to the one anticipated for a PUEO upgrade. The fiber used was identical to the 100 μm core diameter, low-OH, hydrogenated CeramOptec

FIG. 3.—*Left*: FlyEyes dewar. *Right* Mounted on PUEO (ringlike structure at the top) at the Cassegrain focus of CFHT; the dewar in the middle is the KIR scientific imaging camera. See the electronic edition of the *PASP* for a color version of this figure.

step-index fiber used to guide light to the APDs in PUEO. Two methods were considered in constructing the fiber bundle. Each involved precise positioning to match the center spacing of the unit cells, 360 μm $\times$ 560 μm. The first method utilized silicon v groove blocks to form a fiber stack. V grooves in the spacers were etched to match unit cell spacing (Fig. 4 [*right*]). Ultimately, the silicon v-groove method was chosen simply because the v grooves had already been fabricated and were available.

Fixtures were developed to align and hold the fibers and v grooves in place while bonding the fibers. Alignment of the individual silicon v-groove blocks proved to be very difficult. The fiber bundle was aligned by registering the cleaved edges of the v-groove blocks. Unfortunately the cleaved edges were not identical or sufficiently consistent, which resulted in shifts in the fiber position from one row to the next. This offset can clearly be seen in the photograph of the bundle as well as the CCID-35 image of the light output from the individual fibers shown in Figure 5.

The second method consisted of epoxying fibers to a metal ferrule with an array of 145 μm holes spaced 360 μm$\times$ 550 μm, as shown in Figure 4 (*left*). The metal ferrule approach would have provided a more precise fiber bundle and will be probably used should PUEO be upgraded. Electrical-discharge machining can easily produce a ferrule with an array of 145 μm conical holes at 360 μm $\times$ 550 μm spacing at relatively low cost.

The other challenge was positioning the fiber bundle above the CCID-35 surface to obtain a spot size that would fit within the unit cell while avoiding interference with the bond wires on the device. The fiber bundle had to be centered to within a few tens of microns in X and Y, and θ had to be controlled for parallelism. An adjustment mechanism designed by GL Scientific using two pairs of wedges provided for a range of $\pm$700 μm in X and Y and for several degrees of rotation in θ. The height of the bundle above the face of the CCD (the Z direction) was fixed and mechanically set to 200 μm in the mount. There were

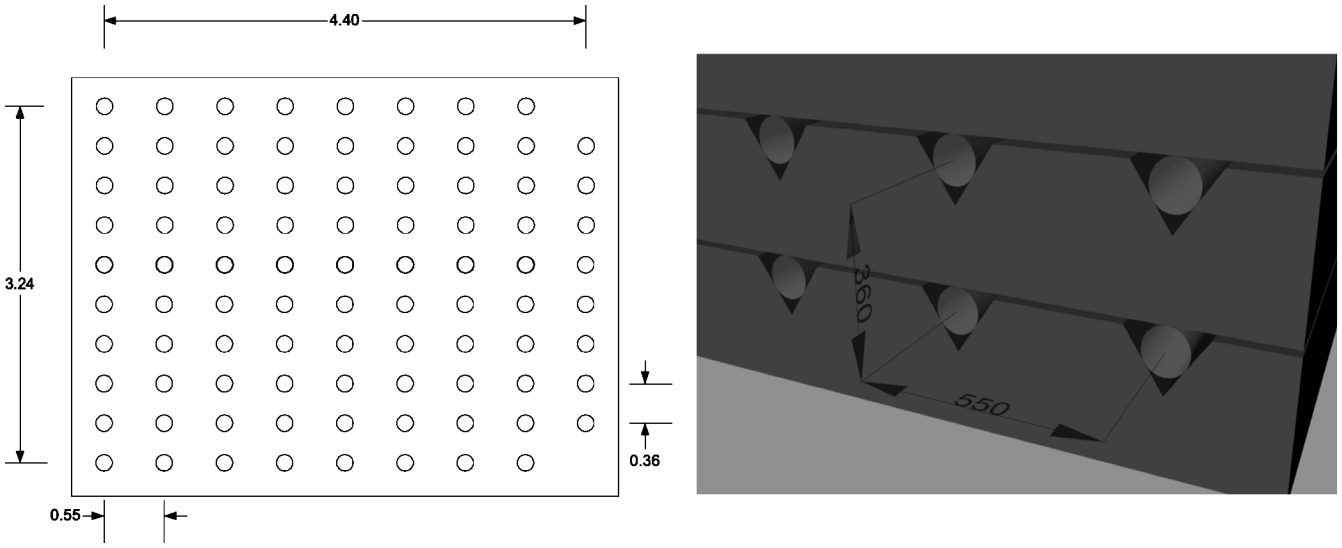

FIG. 4.—*Left*: Ferrule hole pattern (dimensions in millimeters); this method would have provided a more precise fiber bundle. *Right*: Illustration of the stacked silicon v-groove spacers. These ended being used because they had already been fabricated and were available. See the electronic edition of the *PASP* for a color version of this figure.

no provisions for adjustment on the Z axis, although shims could be used to increase the spacing between the fiber bundle and surface of the CCID-35.

The fiber bundle was installed with the CCID-35 operating at room temperature in full frame imaging mode (e.g., Fig. 5 [*right*]). Light was injected into the fibers, and the CCD was read out in real time to provide a streaming video image of the fiber spots. Since there was no way of knowing the alignment of the fiber bundle to the CCD other than through the CCD image itself, a fair amount of caution was used during initial installation. X, Y, and θ were controlled using the adjustment mechanism provided. Z was controlled using a stack of shims that were removed, one at a time, to lower the fiber bundle toward the face of the CCD in a controlled fashion.

In the end, the height of the bundle above the CCD face was close to the 183 μm estimated, and the spots were fairly well centered in the unit cells. During alignment the bundle was removed and installed several times with no apparent shift along any axis. The adjustment mechanism performed well and has been stable after more than 10 cooling and warming cycles. No adjustments have been made since the initial alignment.

One drawback in the design of the fiber bundle was the vacuum feedthrough. By necessity, bare fibers had to be used in vacuum, and jacketed fibers had to be used outside the cryostat. This made for a fiber bundle with a very heavy and fragile end. Several fibers were broken during fabrication and installation because of this. The missing spots in Figure 5 indicate the locations of the broken or poor transmission fibers.

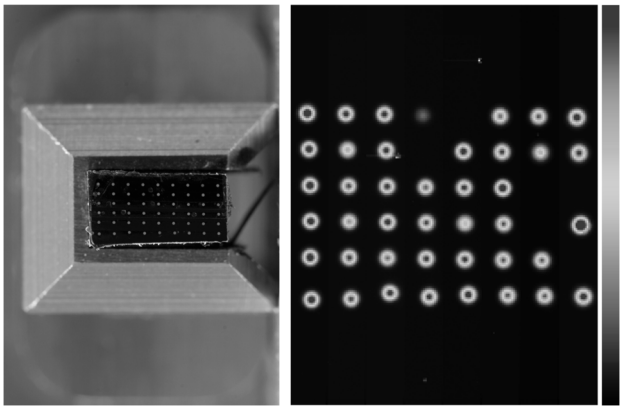

FIG. 5.—*Left*: End view of fibers; 9×6 fiber bundle epoxied into mounting fixture. *Right*: Afocal image of the 8×6 fiber output on the CCID-35, without the tip-tilt columns. Note that the image includes 20 pixels of overscan on the top edge (normally used for noise analysis). Broken or poor transmission fibers can be seen on the top and right sides. See the electronic edition of the *PASP* for a color version of this figure.

2.2. Interface Patch Board

A simple interface board was designed to receive the intrafocal and extrafocal data from the SDSU2 controller and format it for the LaserDot RTC. Previously, the WFS handled these tasks. The design was driven by the constraints of the project: namely, that the current software and hardware interfaces had to be maintained and no modifications to the existing hardware could be made.

In the original PUEO design, the intrafocal (I) and extrafocal (E) pulses from the APDs would clock a multiplex of 38 (19 APDs $\times$ 2) 16-bit up-down counters. Discrete logic would combine the I and E pulses into the sum ($I + E$) and

difference ($I - E$) signals. The sum and difference signals would each clock an individual counter. The output of the counters would be latched and stored in registers on every sampling period (e.g., at 1 kHz). The LaserDot RTC addresses and reads the sums and differences for each APD in 19 32-bit reads and uses these to compute the drive signal to the deformable mirror.

In the new interface board, I and E data from the SDSU2 controller is transmitted down a single fiber and is converted into two parallel words using a HOTlink receiver/converter pair. The data words are written into a first-in/first-out (FIFO) buffer and then stored in a $32\text{K} \times 8$ SRAM. I and E data from 64 of 80 unit cells of the CCID-35 are read regardless of whether they are illuminated with light from the fibers or not, in order to maintain consistent timing between the sampling of different cells. During the commissioning, all the operational fiber and unit cell pairs were examined by viewing the spot image, and the optimal 19 were selected. An address decoder implemented with a complex programmable logic device (CPLD) maps the locations of the best 19 fiber spots to the original LaserDot addresses. By necessity, the interface board uses the same input and output signals and definitions as the WFS. A pair can easily be changed if needed (for instance, if its fiber got broken) by simply remapping the LaserDot RTC addresses to the addresses corresponding to the new pair. This is done through a JTAG port and CPLD programming software. Unlike in the original WFS, the I and E sums and differences are not available, only the raw data. The LaserDot RTC addresses and reads the I and E data and computes the sums and differences in the real-time code.

If PUEO were to be upgraded with FlyEyes, all the electronics and RTC would be redesigned. The present hardware is obsolete and nonscalable. The scheme used on the interface board would not be considered, since it was designed simply to interface with the present hardware. The hardware required would conceivably be much simpler than what was necessary to integrate FlyEyes with PUEO.

2.3. CCID-35 WFS Camera

An image of the fibers on the CCD is shown in Figure 5. Several fibers are broken and a few CCD cells are unusable due to defect structures. For PUEO, only 19 channels are needed, so this does not present a problem. The fibers selected for the signals were from the fibers in the three cell rows nearest the output amplifiers, to minimize the time required to shift out the pixels.

In CFHT's PUEO instrument, the membrane mirror cycles between the intrafocal (I) and extrafocal (E) images at 4 kHz; however, the readout of the photon counts associated with each phase is performed at 1 kHz in its highest-bandwidth operation mode. When the APDs are used for sensing, the system alternates four times per 1 kHz cycle between incrementing the I or E counters. If the sensing frequency is reduced by n octaves, then the system must alternate 4×2^n times between feeding the I or E counters before these are read out. The CCID-35 is clocked in such a way as to emulate this behavior. The readout of the CCID-35 is performed as quickly as possible, within the limits necessary for maintaining low readout noise, in order to minimize the phase lag between the readout of the intrafocal and extrafocal signals.

The unbinned readout noise for this device was previously reported by Ho et al. (2006). Further tests using an alternate measurement method confirmed these results; however, it was found that the noise was significantly higher when binning the pixels 20×20 in AO mode compared with the unbinned imaging mode. It was found that the noise could be significantly reduced (from 3 down to 2 e^- rms) by limiting the swing of the parallel and serial clocks. The most likely explanation for the excess noise at the higher clock swings is spurious charge generation through impact ionization. Although the probability of generating charge in this manner is usually negligibly small at such small voltage swings, the large number of shifts (and fast clock edges) used when operating the device in AO mode (over 80 when sampling at 1 kHz) could lead to a significant effect. The readout noise obtained ranged from 1.9 to 2.7 e^- rms, with an average noise of 2.3 e^- rms.

3. EXPECTED PERFORMANCE AND SIMULATIONS

Although early simulations (Craven-Bartle et al. 2000) show that the performance of FlyEyes should be equivalent to that of the APDs, the read noise of a CCD introduces changes in the operation of a curvature wavefront sensor.

3.1. Read Noise

In photon-counting detectors, the noise on the wavefront sensor measurements is integrated in the servo-loop and low frequencies are more strongly attenuated, due to their improved signal-to-noise ratio (S/N). Thus, with APDs, the variance of the wavefront sensor signal per integration cycle is proportional to N_{phot}^{-1}, where N_{phot} is number of photons detected in a sample time. In a CCD, on the other hand, read noise is added in every frame, so the variance is proportional to N_{phot}^{-2}, where the N_{phot} photons have now been detected in one read (see, e.g., Rousset 1999). This is shown in Figure 6, which shows the variance (and Strehl ratio attenuation) for photon and read-noise-limited wavefront sensors; in a real sensor, the photon noise is added to the read noise, but we neglect this effect, as we only focus on the dominant source of noise in each measurement.

The following equation can be used to calculate the WFS measurement variance for the APDs in which the photon noise dominates (see, e.g., Rousset 1999. eq. [5.45], and Rigaut et al. 1998, eq. [1]):

$$\sigma^2_{\text{WFS}} \simeq \frac{\pi^2}{\eta \times \text{QE}_{\text{APD}} \times N_{\text{photon}}} \text{ rad}^2, \quad (1)$$

where η describes the throughput (and wavefront sensor

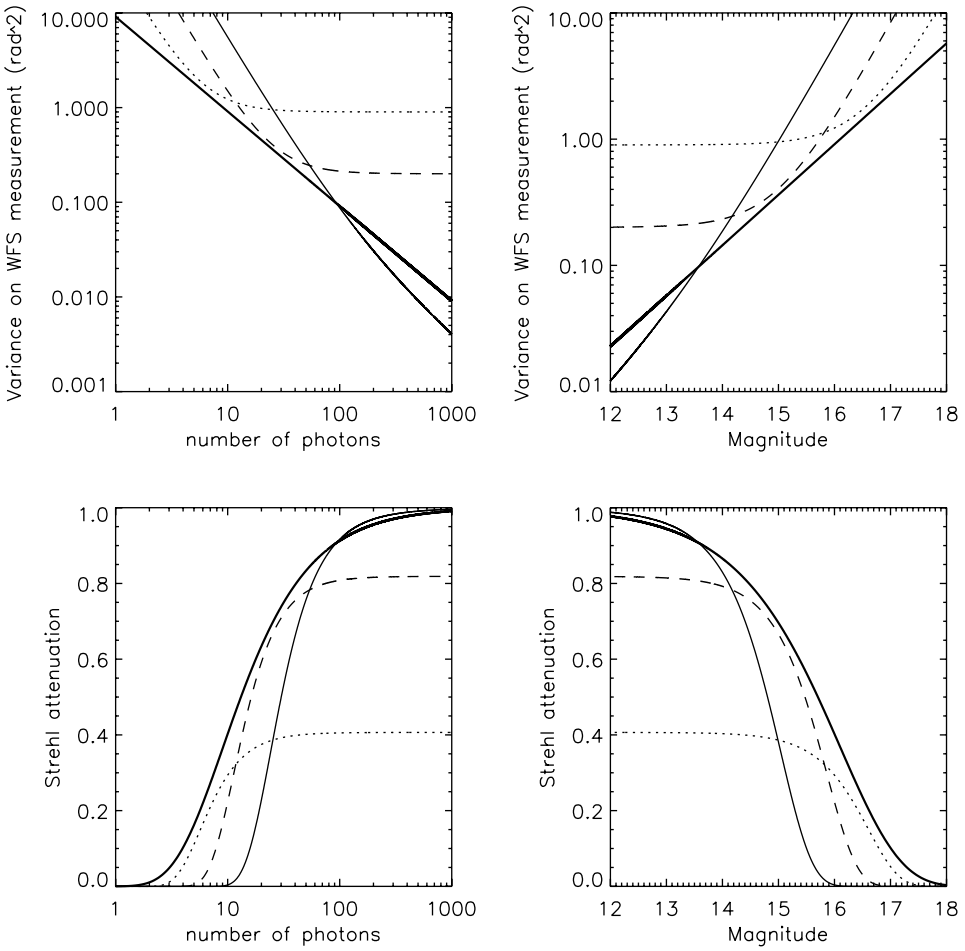

FIG. 6.—Computed variance on WFS measurements (*top*) and equivalent Strehl ratio attenuation (*bottom*) for incident number of photons (*left*) and equivalent guide star magnitude (*right*) for APDs, i.e., photon noise only (*bold line*) and CCID-35 (including read noise at 1 kHz (*solid line*) 500 Hz (*dashed line*), and 250 Hz (*dotted line*).

sensitivity), $N_{\rm photon}$ is the number of photons per integration time, and $\mathrm{QE}_{\rm APD}$ is the APD quantum efficiency: 0.35 in this case. To reproduce PUEO's behavior (see, e.g., Rigaut et al. 1998, Fig. 9), we find that for the throughput to the APDs, $\eta = 0.16$; this provides the proper Strehl ratio attenuation (50% at magnitude 15.7), as measured experimentally. For the CCID-35, we can derive the WFS measurement variance from Rousset (1999), eqs. 5.46, 5.42, and 5.43, as

$$\sigma^2_{\rm WFS} = \pi^2 \frac{(\sigma_{\rm read} \times n_{\rm pixels})^2}{(\eta \times \mathrm{QE}_{\rm CCD} \times N_{\rm photon})^2} + \sigma^2_{\rm bandwidth}\ \mathrm{rad}^2, \qquad (2)$$

where the read noise per pixel $\sigma_{\rm read}$ is 2.3 e^-, read over $n_{\rm pixels}$ (we assume two: one for the intrafocal read and the other for the extrafocal read), where $N_{\rm photon}$ is the number of photons per unit time, and $\mathrm{QE}_{\rm CCD}$ is the CCID-35 quantum efficiency, assumed to be 0.9. We neglect the photon noise term, which only becomes dominant at very high photon flux, and the last term, $\sigma^2_{\rm bandwidth}$, is the phase-lag error. This term is required because although increasing the integration time on the WFS improves the S/N in terms of detected photons, it does so at the expense of the temporal error, determined by the Greenwood frequency and the loop-correction frequency. In the example shown in Figure 6, the CCID-35 is operated at 1 kHz with no phase-lag error, at 500 Hz (double the number of photons per exposure) with a 0.2 rad^2 phase-lag error, and at 250 Hz with a 0.9 rad^2 phase-lag error. This figure illustrates that on the bright end, the improvement in QE allows an improvement in the performance with respect to APDs, while at the faint end (where the read noise starts to dominate), the APD performance level can be emulated by lowering the sampling frequency: the performance at 500 Hz becomes better than at 1 kHz at magnitude 14, and it improves again by going to 250 Hz at around magnitude 16. The preceding formulas make no assumptions as to the exact form of the noise, but compare simple empirical models with the same constants, and so these results strongly imply

that by carefully adjusting the wavefront sensor frequency, the performance of the APDs on PUEO can be matched when using the CCID-35.

3.2. Low Flux Levels

Another difference introduced by the finite read noise of the CCD appears at very low flux levels. The wavefront sensor estimates the local wavefront curvature by estimating the contrast between the intra/extrafocal images:

$$C = \frac{I_{\text{intra}} - I_{\text{extra}}}{I_{\text{intra}} + I_{\text{extra}}} \propto \nabla^2 \phi. \tag{3}$$

In the absence of read noise, the denominator can only be zero when the numerator is also zero, and so if no photons are detected during an integration cycle, we set C to zero. But in the presence of read noise, the denominator can be null or negative once the bias level has been subtracted out (it turns out to be less of a problem if it is negative rather than null). Various schemes were simulated to try to reduce the instability and to improve poor performance at low flux. These included clipping the denominator to positive values only, using a running average on the denominator, and adding a bias to the detected intensities. Results of Monte Carlo simulations using the IDL code simul.pro developed by François Rigaut (2002, private communication) are presented in Figure 7.

Clipping the denominator made the loop unstable and was not pursued. It is apparent that a running average in the denominator only marginally improves the performance, if at all. Adding a bias seems to have a more important effect: the bias subtracts out in the numerator, but adds a constant term in the denominator, effectively lowering the loop (or integrator) gain. As all the simulations were run with a constant loop gain of 0.6, adding a bias to the detector signal improves the results of the simulations at low photon flux. However, PUEO uses a modal control that self-optimizes in closed loop and applies the gain that reduces the residual phase variance. Therefore, when this method was tried on sky, it was not found to improve performance.

Sky testing revealed that the detailed modeling presented previously, which should have predicted the optimal wavefront sensing frequency as a function of the guide star brightness, did not take into account the varying sky conditions. Even accounting for r_0 fluctuations did not allow us to definitively and repeatedly demonstrate an improvement of performance on faint sources at lower sampling frequencies. This may have been due to a rapidly varying atmospheric conditions or very short correlation times, τ_0.

4. ON-SKY PERFORMANCE

FlyEyes was tested on PUEO on the nights of 2007 April 24–26 on bright guide stars and on 2008 February 25–27 over a range of guide star brightness, and a comparison run with the APDs took place on 2007 December 17–18. The comparison tests indicate that the bright star performance is unaffected, as shown in Figure 8. It shows the delivered Strehl ratio as a function of the r_0 (in centimeters) at the wavelength of observation. The crosses show the original 1996 integration data, which consisted of more than 300 observations of stars at all wavelengths in varying conditions (Rigaut et al. 1998). The diamonds show the dynamic Strehl ratio, that is the Strehl ratio attenuation due to the dynamic turbulent component (i.e., corrected of static aberrations) measured on images obtained with KIR (the science camera) in 2007 April as a function of the r_0 estimated from the wavefront sensor data, and they are right at the expected value. Experiments with the various schemes described in § 3.2 were carried out, but it was found that the loop remained most stable with no modifications (i.e., no bias or running average).

Images of the guide stars were recorded in the K band on the KIR infrared camera, and standard data-reduction techniques were applied to extract the PSF and measure the Strehl ratio. The comparison with APDs turned out to be more difficult than anticipated, due to varying seeing (and τ_0) conditions, leading to a very large spread of performance for a given magnitude. Nonetheless, by recording the wavefront sensor data simultaneously to the images during the 2008 February observing run, using it to estimate the r_0, and comparing it with our model and the original 1996 integration data, we were able to confirm that the performance was not noticeably degraded by using FlyEyes instead of the APDs.

The modal control of PUEO works by estimating the input-phase temporal power spectrum for each mode from measuring the residual power spectrum of the WFS measurement and using a model of its well-known and characterized closed-loop transfer function. Once the input spectrum is estimated, the loop gain (which minimizes the integral of the product of this spectrum multiplied by the associated error transfer function) is determined. This gain is applied to the loop and the whole process is repeated; the loop gain thus self-optimizes in closed loop. This process depends on the transfer function used, and in PUEO, the temporal characteristics of the integrator and the photon noise make this a straightforward process. We were unable to implement a full modal control for FlyEyes, as the closed-loop transfer function associated with this detector was unknown and it would have required modeling (or measuring) the transfer functions and the read noise for the different sampling frequencies and loop gains with little certainty in their accuracy. Instead, we ran our tests with either the modal control enabled (assuming the simplest loop integrator, but neglecting read noise, and thus probably not optimized) or with zonal control enabled, setting the gain manually. This made the testing cumbersome, but a sufficient number of data points were collected to see trends emerging, as shown in Figure 9.

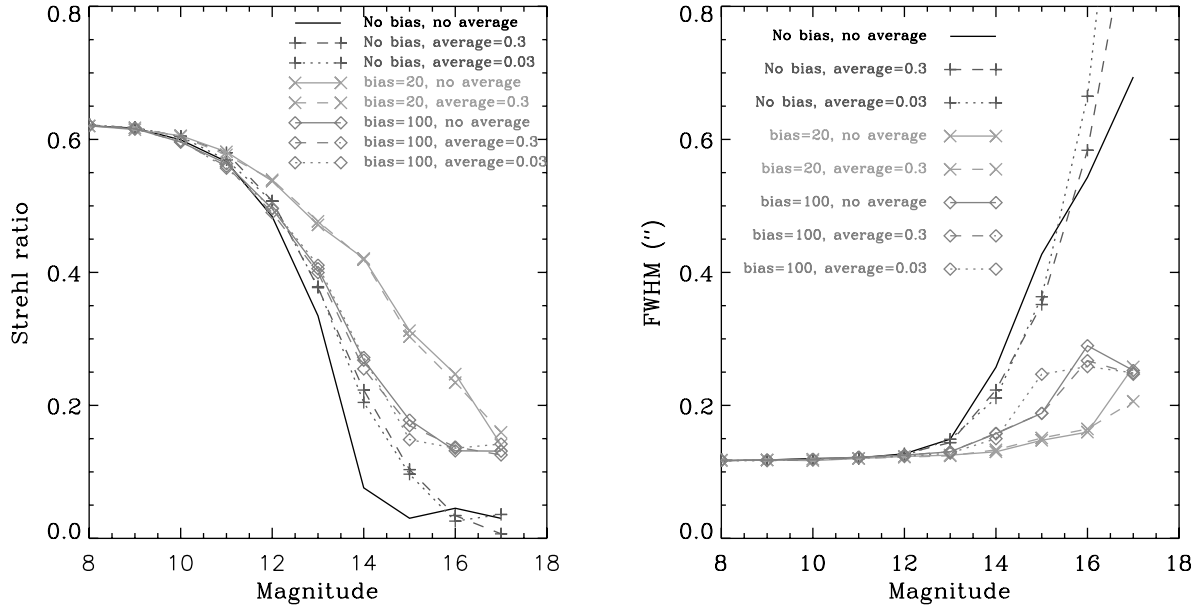

FIG. 7.—Simulated Strehl ratio and FWHM as a function of guide star magnitude, with bias or running average in denominator to prevent loop instabilities. A bias of 20 seems to provide the most improvement in this case.

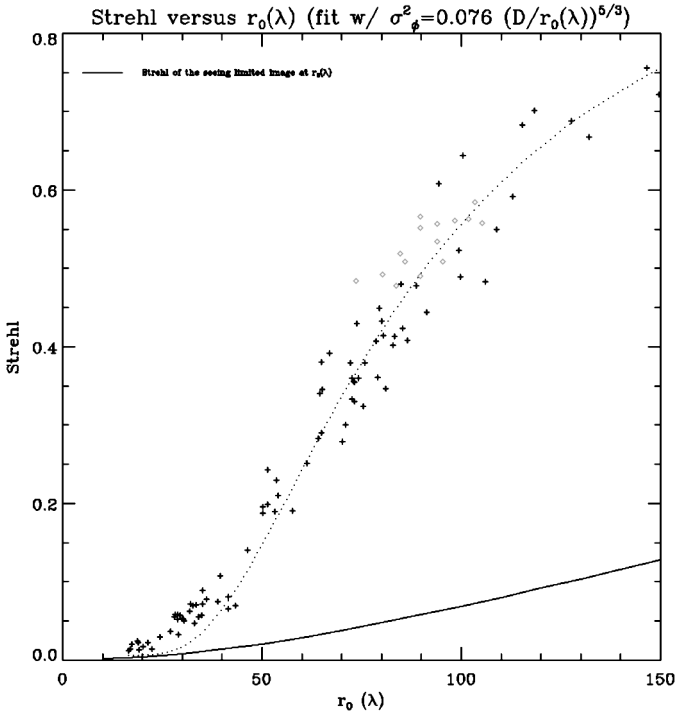

FIG. 8.—Bright guide star performance, showing the delivered Strehl ratio as a function of r_0 expressed in centimeters at the wavelength at which the Strehl ratio is measured (λ); original 1996 integration data (*crosses*), 2007 April data (*diamonds*). The performance is unaffected by FlyEyes. See the electronic edition of the *PASP* for a color version of this figure.

The top row in Figure 9 shows the number of detected photons translated into magnitudes as a function of the quoted guide star magnitude. Some spread can thus be expected due to varying spectral type and photometric conditions. The zero point of 18.5 is the same for FlyEyes as it is for the APDs (Rigaut et al. 1998). The black $\times$ symbols are for 1 kHz data, the gray $+$ symbols are for 500 Hz, and the light gray $\diamond$ symbols are for 250 Hz. Note that the read noise seems to appear at magnitude 15.4 at 1 kHz. Due to the improved QE of FlyEyes, one would expect the zero point to be 0.75 mag larger; the fact that there appears to be no noticeable improvement points to the fact that the throughput to FlyEyes is not as efficient as expected. The most likely culprit for this loss of flux is the extra connector and length of fiber that are added to switch from the APDs to FlyEyes. A set of extension cables for the APDs was designed and built, but the only time they were used was under poor photometric conditions, so a direct comparison is not available to us. Nonetheless, these sky results imply that for FlyEyes, the value of η should be closer to 0.08.

The middle row in Figure 9 shows the raw K-band Strehl ratio, as measured on the KIR detector as a function of the guide star magnitude. The spread is understandable, as there is no accounting for either the actual detected number of photons or the r_0 at the time of the observations. The left panel shows modal control and the right panel shows zonal control; as discussed previously, in both cases the black $\times$ symbols represent the 1 kHz sampling frequency, the gray $+$ symbols show 500 Hz, and the light gray $\diamond$ symbols show 250 Hz. The spread is such that it is hard to infer any quantitative assessment of the performance, although qualitatively, it would appear that

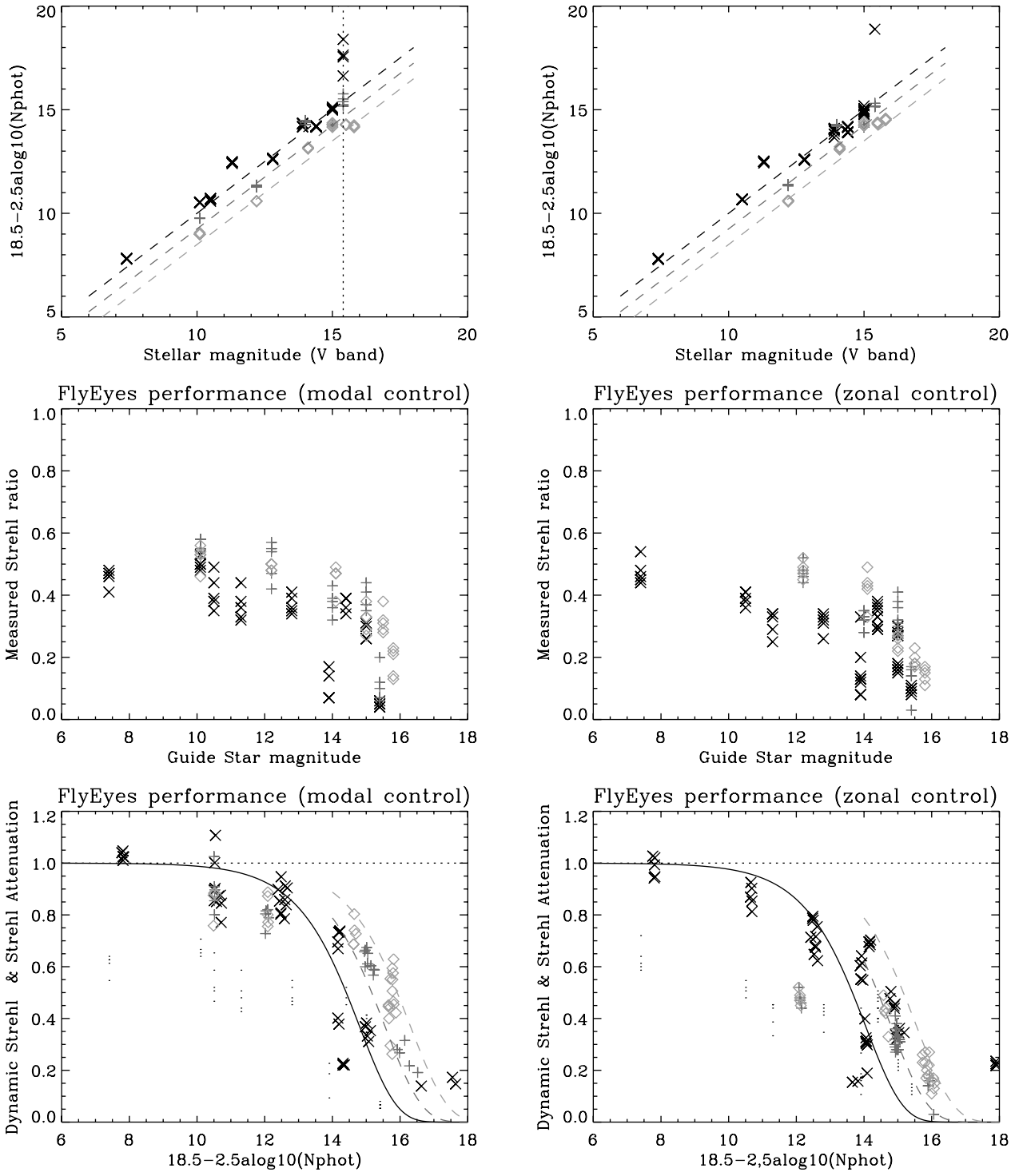

FIG. 9.—FlyEyes performance as a function of guide star magnitude. *Left*: PUEO modal control. *Right*: Zonal control at various gains. *Top*: Photometry. *Center*: Measured Strehl ratio on IR camera. *Bottom*: Strehl ratio attenuation, corrected for r_0; 1 kHz, (*black* ×), 500 Hz (*gray* +), and 250 Hz (*light gray* ⋄)—see text for details.

lowering the sampling frequency ought to improve the performance above magnitude 11. This is misleading, however, as the 1 kHz performance is much lower than the expected 60% that PUEO routinely delivers on bright stars in the K band (e.g., Fig. 8). To be comparable, these data points have to be corrected for the Strehl ratio attenuation due to the instantaneous r_0. This

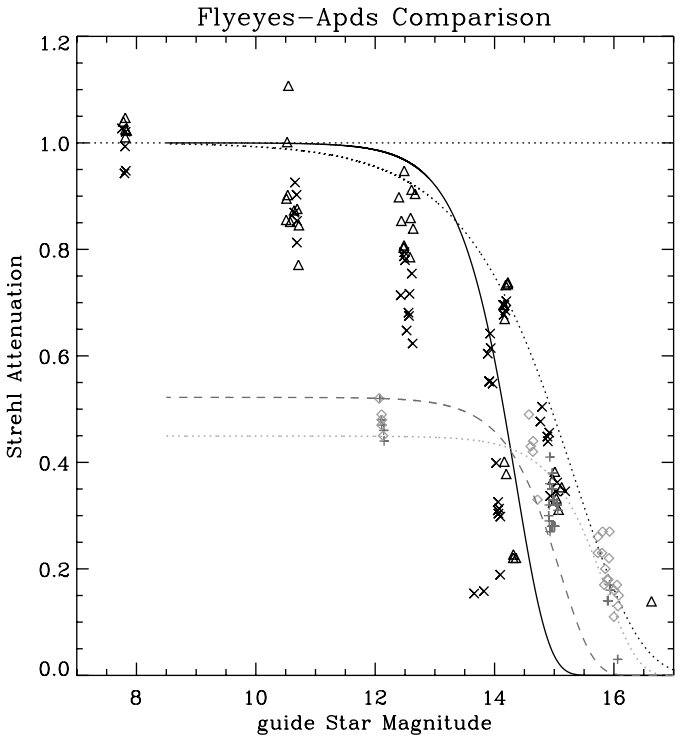

FIG. 10.—Comparison of FlyEyes modal (1 kHz [*black* △]) and zonal control performance (1 kHz [*black* ×], 500 Hz [*gray* +], and 250 Hz [*light gray* ◇]) as a function of guide star magnitude compared with APDs model from Fig. 6. FlyEyes model (*solid line*), FlyEyes 500 Hz model (*light dashed line*), FlyEyes 250 Hz model (*light dotted line*), PUEO APDs model with $\eta = 0.08$ (*black dotted line*). The discrepancy around magnitude 10–12 can be attributed to a poorly tuned loop or very fast atmosphere, but the critical crossover behavior occurs between magnitudes 14 and 16.

is achieved by using a fit of the Strehl ratio attenuation as a function of $r0$ (as in Fig. 8).

The bottom row in Figure 9 shows the final result, after having accounted for the static Strehl ratio (measured on a calibration source), the number of detected photons, and r_0 at the time of the observations. The small black dots are the dynamic (i.e., corrected only for static aberrations) Strehl ratio at 1 kHz, leaving the spread unchanged, but renormalized. The black × symbols show the same data corrected for r_0 and can thus be interpreted as the Strehl ratio attenuation. The gray + symbols show the Strehl ratio attenuation at 500 Hz, and the light gray ◇ symbols are at 250 Hz; the spread of the data is reduced. A best-fit model to the data is shown by the curves (the dashed curves show how much the 1 kHz curve would be displaced if halving the sampling frequency simply doubled the number of photons, assuming a negligible phase-lag error). There is fair agreement, especially for the 250 Hz data at the faint end. Also note that on bright (magnitude 12) stars, the zonal control performs much more poorly at 500 and 250 Hz than at 1 kHz, as was expected (e.g.. Fig. 6). However, in modal control at high flux, the read noise is small compared with the photon and lag noise, so the loop-gain optimizing algorithm seems to be doing the right thing, improving the performance by increasing the loop gain so as to compensate the lower loop frequency. Quantitatively, we can point out that we expect a Strehl ratio attenuation of 50%, due to the guide star brightness at around magnitude 15.

A direct comparison with the APD's performance was not possible, due to the poor seeing and high variability of τ_0 at the time of observations. However, since PUEO's behavior is well understood, the comparison with the model established in § 3.1 is presented in Figure 10. Independently of the estimation of η from the photometry, the throughput and wavefront sensor sensitivity factor η had to be decreased from 0.16 to 0.08 for the APD model to match the 250 Hz and 500 Hz FlyEyes data on faint magnitude. On the bright end (magnitude 10–12), the 1 kHz FlyEyes correction shown on the middle panels of Figure 9 is expected to be around at least 60% in the K band, but is instead found to produce Strehl ratios on the order 30% to 40%; r_0 was measured to be around 10 cm at the time of these observations, and it is thus likely that this poor seeing is partly responsible for the poor performance at these medium magnitudes. This discrepancy can also be due to poorly tuned zonal loop gain, as is shown by the modal control points at 1 kHz, which are all very close to the expected curve (with $\eta = 0.08$).

We therefore infer that the throughput, η, is decreased by a factor of 2 with FlyEyes, and we suspect the extra connector and fibers. We developed a new fiber bundle to be used with the APDs that replicated the FlyEyes fiber bundle (with an extra connector and extra fiber length), but the quality of the data acquired with the APDs was not good enough to allow a direct comparison and determine η independently. In addition to the expected connector losses, it is also possible that the throughput of PUEO has decreased over the 14 years since commissioning. What is important for our purposes is that the same value for η is used in the comparison between the APDs and FlyEyes, as getting rid of the extra connector in FlyEyes should restore η to its APD level of 0.16.

The values for $\sigma_{\text{bandwidth}}$ are very roughly estimated at 0.65 rad^2 for 500 Hz and at 0.8 rad^2 for 250 Hz, although these values are expected to be highly dependent on τ_0 and the wavefront sensor estimation of r_0. These values will also have a large effect on the sampling frequency crossover magnitudes, which our data are not quite accurate enough to resolve, but we do find that reducing the sampling to 500 Hz at around magnitude 15 and to 250 Hz at magnitude 16 improves the performance with respect to 1 kHz, roughly as expected from Figure 6, and allows us to regain the APD's performance, which is shown by the dotted line in Figure 10. FlyEyes provided a (measured) Strehl ratio of 25% at 250 Hz on a magnitude 15.8 star for a short period.

Even though a direct comparison with the APDs was not possible, these FlyEyes results are at least as good as the model of

our APDs from commissioning data if we assume the same throughput η for both. This conclusively demonstrates that a CCD-based detector can successfully be used to replace APDs in curvature sensing, and although the decreased demand on PUEO implies that there is no immediate motivation to do so, FlyEyes is ready to be integrated to PUEO. An upgrade of PUEO is now easily within reach, should the astronomical community support it.

5. CONCLUSION

We have described the FlyEyes experiment, which used a CCID-35 CCD detector as an alternate detector to PUEO's APDs. The CCID-35 has better quantum efficiency than the passively quenched APDs used in PUEO, but introduces a 2 e^- read-noise penalty. Ideally, the absence of read noise (of APDs or EMCCDs) allows us to optimally reconstruct the wavefront for each spatiotemporal wavefront coherence volume (i.e., within r_0 and τ_0). Adding read noise makes the control optimization more complicated, as the frame rate has to be adjusted to maintain a useful S/N per subaperture and per measurement. Therefore, one can expect that when increasing the order of the system (i.e., smaller subapertures), the loop frequency will have to be decreased to properly correct the wavefront at constant flux, and the correction will fail as the temporal error increases and becomes dominant; effectively, in the presence of read noise, the limiting magnitude will decrease as the order of the system increases. For our purposes, the level of read noise (2 e^-) was sufficiently small, compared with other sources of error.

FlyEyes was successfully integrated and tested with PUEO using a fiber bundle to divert the light from the APDs to a CCID-35 detector. An interface board was implemented to send the WFS measurements to the real-time computer. On-sky operation was achieved on bright stars ($V < 10$). On fainter stars ($10 < V < 16$), different schemes were attempted to reduce the effects of the read noise, but none showed definitive improvements under our test conditions. FlyEyes performed at least as well as APDs, although varying atmospheric conditions made it difficult to establish performance as a function of guide star magnitude. Quantitatively, a Strehl ratio attenuation of 50% can be expected when the guide star is magnitude 15; this is also the crossover frequency where 500 Hz improves the performance with respect to 1 KHz. At around magnitude 16, decreasing the sampling frequency to 250 Hz improves the correction again. Anecdotally, FlyEyes provided a 25% Strehl ratio on a 15.8 mag star. The demand for PUEO is steady but low, so there is no strong incentive to use FlyEyes as a replacement for the APDs, as this would require further effort into integrating FlyEyes into PUEO and improving the reliability and automation of the performance optimization. However, an upgrade of PUEO is now within reach: curvature AO systems with 100–200 subapertures are now operating with spectacular success, and the results presented in this article show that it is now possible to reduce their cost substantially by replacing the APDs with CCDs.

REFERENCES

Beletic, J. W., Dorn, R. J., Craven-Bartle, T., & Burke, B. 2000, in 4th ESO CCD Workshop, Optical Detectors for Astronomy II: State-of-the-Art at the Turn of the Millennium (Dordrecht: Kluwer), 283

Craven-Bartle, T. V., Dorn, R. J., & Beletic, J. W. 2000, Proc. SPIE, 4007, 444

Cuillandre, J.-C., Beletic, J. W., Dorn, R. J., Luppino, G. A., Isani, S., Gorceix, N., Lai, O., Craven-Bartle, T. V., et al. 2003, Proc. SPIE, 4839, 272

Dorn, R. J. 2001, Ph.D. dissertation, Ruperto-Carola Univ. (Heidelberg)

Feautrier, P., Gach, J-L., Balard, P., Guillaume, C., Downing, M., Hubin, N., Stadler, E., Magnard, Y., et al. 2010, Proc. SPIE , 7736, 77360Z

Ho, K. J., Cuillandre, J. C., Lin, C. J., Benedict, T., Lai, O., Ward, J., Salmon, D., Luppino, G., et al. 2006, Proc. SPIE, 6276, 62761G

Ho, K., Cuillandre, J.-C., Puget, P., Salmon, D., Lai, O., Beletic, J. W., Luppino, G., Dorn, R. J.et al. 2004, Proc. SPIE, 5499, 395

Lai, O. 2004, On-Line Proc. PUEO NUI Workshop (Grenoble: LAOG), http://www.cfht.hawaii.edu/Instruments/Imaging/AOB/Workshop/Proceedings/proceedings.html

Lai, O., Ménard, F., & Cuillandre, J.-C. 2003, Proc. SPIE, 4389, 659

Racine, R. 2006, PASP, 118, 1066

Rigaut, F. J., Salmon, D. S., Arsenault, R. A., Thomas, J., Lai, O., Rouan, D., Véran, J.-P., Gigan, P., et al. 1998, PASP, 110, 152

Rousset, G. 1999, in Adaptive Optics in Astronomy, ed. F. Roddier (Cambridge: Cambridge Univ. Press), 91

Thomas, S. J., Adkins, S., Gavel, D., Ellerbroek, B., Gilles, L., & Fusco, T. 2008, MNRAS, 387, 173